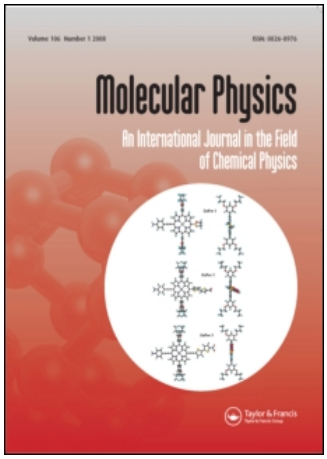

Molecular Physics
An International Journal in the Field of Chemical Physics
Publication details, including instructions for authors and subscription information:
http://www.informaworld.com/smpp/title~content=t713395160

Photodissociation of vibrationally excited OH/OD radicals

Dragana Č. Radenović [a]; André J. A. van Roij [a]; Shiou-Min Wu [a]; J.J. Ter Meulen [a]; David H. Parker [a]; Mark P. J. van der Loo [b]; Liesbeth M. C. Janssen [b]; Gerrit C. Groenenboom [b]
[a] Molecular and Laser Physics, IMM, Radboud University Nijmegen, Nijmegen, The Netherlands
[b] Theoretical Chemistry, IMM, Radboud University Nijmegen, Nijmegen, The Netherlands

Online Publication Date: 01 January 2008
To cite this Article: Radenović, Dragana Č., van Roij, André J. A., Wu, Shiou-Min, Meulen, J.J. Ter, Parker, David H., van der Loo, Mark P. J., Janssen, Liesbeth M. C. and Groenenboom, Gerrit C. (2008) 'Photodissociation of vibrationally excited OH/OD radicals', Molecular Physics, 106:2, 557 - 572
To link to this article: DOI: 10.1080/00268970801922783
URL: http://dx.doi.org/10.1080/00268970801922783

Molecular Physics
Vol. 106, Nos. 2–4, 2008, 557–572

RESEARCH ARTICLE

Photodissociation of vibrationally excited OH/OD radicals

Dragana Č. Radenović[a], André J.A. van Roij[a], Shiou-Min Wu[a], J.J. Ter Meulen[a], David H. Parker[a]*, Mark P.J. van der Loo[b], Liesbeth M.C. Janssen[b] and Gerrit C. Groenenboom[b]

[a]*Molecular and Laser Physics, IMM, Radboud University Nijmegen, Toernooiveld 1, 6525ED, Nijmegen, The Netherlands;* [b]*Theoretical Chemistry, IMM, Radboud University Nijmegen, Toernooiveld 1, 6525ED, Nijmegen, The Netherlands*

(*Received 12 October 2007; final version received 10 December 2007*)

This paper describes a joint experimental and theoretical study of the photodissociation of vibrationally excited hydroxyl radicals. OH and OD radicals produced in a pulsed electric discharge supersonic beam are state-selected and focused by a hexapole and then photo-dissociated by a single laser tuned to various H/D or O atom $(2+1)$ resonance enhanced multiphoton ionization (REMPI) wavelengths between 243 nm and 200 nm. The angle velocity distributions of the resulting O^+ and D^+ photofragment ions were recorded using velocity map imaging. Photodissociation to the $O(^3P_J)+H(^2S)$ limit is shown to take place by one-photon excitation to the repulsive $1\ ^2\Sigma^-$ state. The experimental data shows that vibrationally excited OH/OD which are formed in the discharge are dissociated, and a vibrational temperature of $\approx$2000 K was estimated for the beam source. An analysis in the high-energy recoil sudden limit is used to predict the $O(^3P_J)$ fine structure branching ratios and alignment information in the molecular and laboratory velocity frame of the imaging experiment. The measured and predicted fine structure branching ratios and alignment parameters agree well at all dissociation wavelengths, supporting the model for photodissociation in the sudden limit regime. Several aspects of the experiment such as OH pre-alignment and orientation, ion-recoil, and Doppler-free imaging are discussed.

Keywords: hydroxyl radical; photodissociation; state selection; atom polarization; sudden limit model

1. Introduction

Due to its central role in the photochemistry of the Earth's atmosphere, in combustion processes and in the interstellar medium, the spectra and photodynamics of the highly reactive hydroxyl radical (OH) has been the subject of numerous theoretical and experimental investigations. A wealth of detailed theoretical predictions for the photodissociation dynamics of OH is available from studies using high-quality *ab initio* calculations of the OH electronic structure. Despite its importance, experimental studies of OH photodissociation under collision-free conditions have only recently been reported [1, 2].

Examination of the OH potential energy curves, Figure 1, for the optically accessible excited electronic states reveals why laboratory studies of OH photodissociation are so challenging. Given the O–H bond dissociation energy, D_0, of 4.37 eV [3], photodissociation of OH can in principle occur at wavelengths shorter than 284 nm. Transitions to vibrational levels $v' \geq 1$ of the $A\ ^2\Sigma^+$ state from the $X\ ^2\Pi$ ground electronic state, which lie in the ultraviolet (UV) region of the spectrum and are used for laser induced fluorescence detection of OH, lead to predissociation, producing $O(^3P)+H(^2S)$ atoms. Van Dishoeck and Dalgarno [4] have shown that the total dissociation yield for this $A\ ^2\Sigma^+ \leftarrow X\ ^2\Pi$ transition is much smaller ($\approx 10^{-5}$) than photodissociation from the higher energy electronic states, thus the $A\ ^2\Sigma^+ \leftarrow X\ ^2\Pi$ channel (when starting from the lowest vibrational levels of the X state) is in most circumstances of no importance in the total photodissociation process.

All of the remaining allowed electronic transitions, to the repulsive $^2\Sigma^-$, $^2\Delta$, and $^2\Pi$ upper states that dominate photodissociation of OH, lie in the vacuum ultraviolet (VUV) spectral region where intense laser sources are not readily available. VUV photodissociation is the main destruction process of OH in diffuse clouds in the interstellar medium, where VUV radiation is intense [5, 6]. Besides the VUV difficulty, most sources of OH radicals also co-produce large amounts of $O(^3P_J)$ and $H(^2S)$ atoms, which can overwhelm the detection of photo-product signals.

Using an electrostatic hexapole lens to concentrate and state-select our electric discharge driven OH beam [7] in combination with the velocity map imaging

*Corresponding author. Email: parker@science.ru.nl

ISSN 0026–8976 print/ISSN 1362–3028 online

DOI: 10.1080/00268970801922783
http://www.informaworld.com

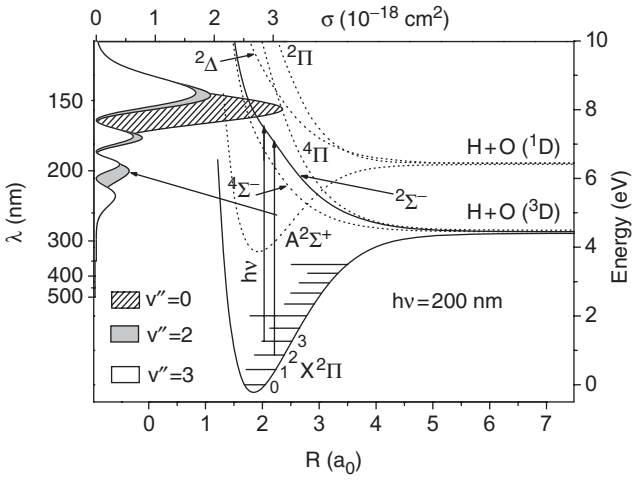

Figure 1. Potential energy diagram of the OH electronic states relevant to this study. On the left side of the figure are photodissociation cross-sections for excitation from the vibrational levels $v''=0$, 2 and 3 of the ground ($X\ ^2\Pi$) electronic state to the repulsive $1^2\Sigma^-$ state of OH from 100 to 350 nm. The vertical arrows represent one-photon dissociation at ≈200 nm of the repulsive $1^2\Sigma^-$ state from the vibrational levels $v''=2$ and 3 of the ground state of OH. At 200 nm, for example, the photodissociation cross-section from $v''=2$ is larger than that from $v''=3$.

detection technique [8], we have succeeded in observing direct photodissociation of state-selected OH/OD through the first repulsive $1\ ^2\Sigma^-$ state under collision-free conditions, with state-specific detection of the D and O atom products [1]. The OH beam source [7] produces small amounts of vibrationally excited OH, and the internal vibrational energy, E_{vib}, allows photodissociation by UV instead of VUV radiation, where $h\nu_{UV}=h\nu_{VUV}-E_{vib}$. Due to the very low amounts of the higher vibrational states in the molecular beam, it was necessary to perform a one-laser experiment, where a single laser beam is used for both photodissociation of OH and detection of the O or H photo-products. This provides higher sensitivity but less flexibility than a two-laser experiment. With this approach, we have carried out a series of studies of direct photodissociation of OH and OD [1] as well as the isovalent molecules SH and SD [9]. A two-laser dissociation-probe scheme (exciting the most pop^{2}ulated $X^2\ \Pi$ ($v''=0$) level) is also being used in our laboratory to study predissociation of the $A\ ^2\Sigma^+$ state of all four molecules. Using the high resolution H atom Rydberg tagging method, Zhang and co-workers have reported $A^2\Sigma^+$ state predissociation of OH/OD [2] and direct UV photo-dissociation of SH/SD [10] and the results of these two different but complementary experimental approaches are compared in this paper.

A previous Communication [1] described photodissociation of OD radicals using velocity map imaging to probe the speed and angular distribution of the D(^{2}S) products formed by photodissociation of OD at 243 nm, and the O($^3P_2$) atom products of OD photodissociation at 226 nm. This paper describes extended studies of state-selected D ($n=1,^2$S) atom detection from OD at 243 nm as well as at 205 nm, along with studies of the different $J=2$, 1, 0 fine structure states of the O(^3P_J) atoms following photodissociation of OD and OH at 226 nm and 200 nm. Doppler-free imaging of OD photodissociation with D atom detection at 243 nm and ion-recoil effects in OH/OD photodissociation imaging is also described. We show from experiment and first principle calculations that our images are due to one-photon dissociation to the first dissociation limit of vibrationally excited OH/OD molecules through the repulsive $1\ ^2\Sigma^-$ state. One-photon dissociation to the second dissociation limit, producing O(^{1}D) atoms, was not observed in this work, but this channel was clearly observed and characterized in the UV photodissociation of the SH and SD molecules, as reported previously [9]. The O(^{1}D) channel from OH is the subject of ongoing investigation in our laboratory.

2. Photodissociation of OH

Ab initio potential energy curves for the ground and lower electronically excited states of OH ($X^2\Pi$, $A\ ^2\Sigma^+$, $1\ ^2\Sigma^-$, $1\ ^4\Sigma^-$, $1\ ^4\Pi$, $1\ ^2\Delta$, $2\ ^2\Pi$) calculated by van der Loo and Groenenboom [11] are presented in Figure 1. In the OH $X^2\Pi$ ground state (Hund's case b) the $^2\Pi_{3/2}$ spin–orbit component is 123 cm^{-1} lower in energy than $^2\Pi_{1/2}$ [12]. The OH $X^2\Pi$ ground state and the $1\ ^2\Sigma^-$, $1\ ^4\Pi$, and $1\ ^4\Sigma^-$ repulsive states correlate adiabatically with ground state product atoms O(^3P_J) + H($n=1,^2$S), while the first excited bound state $A^2\Sigma^+$, and the repulsive states $1\ ^2\Delta$ and $2\ ^2\Pi$ correlate with the second dissociation limit [O($^1D_2$) + H($n=1,^2$S)]. Van Dishoeck and Dalgarno [4] showed that absorption to the repulsive $1\ ^2\Sigma^-$, $^2\Delta$, and $^2\Pi$ states corresponds to strong, broad bands in the VUV region of the spectrum peaking at 7.81, 9.79, and 11.25 eV, respectively. They pointed out that direct photodissociation via the $1\ ^2\Sigma^-$ state (which is repulsive at all distances) is the major destruction mode for OH in diffuse interstellar clouds and in comets [6]. Yarkony [13] and others [14] have predicted the final product quantum state distributions for direct dissociation and pre-dissociation of OH, which in general follow the expectations for a 'sudden limit' diabatic process. Lee [15], however, predicted large

deviations from the sudden limit model due to interference effects from simultaneous absorption to the repulsive wall of the $A^2\Sigma^+$ state and the $1\ ^2\Sigma^-$ repulsive state. Most recently, van der Loo and Groenenboom [11] reported refined potential energy curves for the $X^2\Pi$, $A^2\Sigma^+$, $1\ ^2\Sigma^-$ and several high-lying Rydberg states of OH, which we use in this study to explain the photodissociation dynamics of OH excited to the $1\ ^2\Sigma^-$ excited electronic state.

The potential energy curves, position of ro-vibrational levels, transition dipole moments, etc., are very well determined for the OH $X^2\Pi$ and $A^2\Sigma^+$ electronic states. In a separate study, we will report velocity map imaging of the $O(^3P_J)$ products formed by predissociation of OH $A\ ^2\Sigma^+$ ($v'=3$, $N'=0$, 1 and 2). We have also reported two-photon resonance enhanced multiphoton ionization, (2 + 1) REMPI, of vibrationally excited OH and OD via the $D^2\Sigma^-$ and $3\ ^2\Sigma^-$ Rydberg states [16]. From this knowledge we can state that the energies of the photons in this UV photodissociation study are not resonant with any known one-photon $A^2\Sigma^+ \leftarrow X^2\Pi(v'')$ transition, or any known two-photon transitions to the $D^2\Sigma^-$ or $3\ ^2\Sigma^-$ Rydberg states. In this work, photodissociation is a direct one-photon process and for the photon energies used only one upper electronic state is of importance, the repulsive $1\ ^2\Sigma^-$ state.

As the OH $1\ ^2\Sigma^-$ state correlates adiabatically with the $O(^3P_0) + H(^2S)$ limit [15], at the threshold for photodissociation these are the only products expected. However, as seen in Figure 1, Franck–Condon overlap limits absorption from the lower vibrational states of the OH X state only to excited electronic states lying well above the first dissociation limit. OH photodissociation is most likely a diabatic process due to this large excess energy, and due to the small mass and thus high velocity of the recoiling H atom. In the diabatic picture, the electronic Hamiltonian (without spin–orbit coupling) is diagonalized and spin–orbit interactions can cause coupling of the diabatic curves along the dissociation coordinate. If the excess energy is much larger than the spin–orbit coupling (among the $1\ ^2\Sigma^-$, $1\ ^4\Pi$, and $1\ ^4\Sigma^-$ repulsive states) there is insufficient time for the electronic and spin angular momentum to recouple at the large internuclear distance. Dissociation is then in the high-energy recoil or 'sudden' limit and takes place essentially on the optically prepared diabatic state. In this limit, the projection of the molecular wave function of the initial diabatic state onto the atomic basis states of the products determines the final product state distribution, and this distribution does not vary with the excitation energy. The UV photodissociation of OH is considered to approach the sudden limit on the diabatic $1\ ^2\Sigma^-$ curve.

Zhang and coworkers [10] studied ultraviolet photodissociation of the isovalent SH radical by detecting H atom products by the high resolution Rydberg tagging time-of-flight (TOF) method. They were able to resolve the three $S(^3P_J)$ channels in the co-fragment H atom TOF signal, and their measured J-dependent branching ratios confirm that dissociation via the $1\ ^2\Sigma^-$ state of SH can be described using the sudden-limit approximation. While our imaging method (here applied to OH) has lower velocity resolution, it can be used to detect both H and O atoms, and provides polarization information (M_J state populations) for the J-state specified $O(^3P_J)$ atom products. This $O(^3P_J)$ polarization data is an important indicator of the pathways for OH photodissociation.

3. Sudden limit analysis of OH photodissociation

Potential energy curves for the $X^2\Pi$ and $1\ ^2\Sigma^-$ states, reported by van der Loo and Groenenboom [11], are used in this section to predict the wavelength-dependent photodissociation cross sections for OH $X(v''=0$–$5)$, and their contribution in the final $O(^3P_J)$ product distributions including polarization information (as prescribed for sudden-limit dissociation) in the molecular body-fixed (J, ω) and laboratory (J, M_J) frame. This analysis is used later in the article for interpretation of and comparison with the experimental data. A sudden limit analysis in the molecular body-fixed (J, ω) and laboratory (J, M_J) frame for photodissociation via the repulsive wall of the $A^2\Sigma^+$ state to the second dissociation limit was carried out in [9] for SH and SD. This analysis is identical for OH and OD and is not repeated here.

3.1. *Photodissociation cross-sections*

Ab initio calculations of the OH/OD ground- and excited-state potential energy surfaces and internuclear distance-dependent dipole transition moments are described in [11]. Briefly, the potential energy curves and dipole transition moments are computed with MOLPRO [17] at the internally contracted multi-reference configuration interaction level [18, 19], with single and double excitations. Orbitals are obtained from complete active space self consistent field calculations [20, 21], using an aug-cc-pV6Z one-electron basis set. We use the sinc-DVR method [22, 23] to compute the nuclear vibrational wave functions and renormalized Numerov propagation to compute the nuclear dissociative wave functions.

The $X^2\Pi$ (v'') vibrational quantum state dependent photodissociation cross section (see Figure 1) σ in cm^2 is given by:

$$\sigma(\omega) = \frac{4\pi^2\alpha\hbar\omega}{3e^2}\left|\left\langle 1^2\Sigma^-, E|\mu_x|X^2\Pi_x(v)\right\rangle\right|^2, \qquad (1)$$

where α is the fine-structure constant, e the elementary charge, ω the frequency of the absorbed photon, E^- the kinetic energy release, μ_x the x-component of the electronic dipole operator, and v the vibrational level of the ground state.

Wavelength-dependent photodissociation cross-sections in cm^2 are plotted on the left side of Figure 1 for photodissociation beginning from the OH X ($^2\Pi$) $v''=0$, 2, and 3 vibrational states. For the OH X ($v''=0$) state, our maximum value of $3.15\times0^{-18}\,cm^2$ for the photodissociation cross section (at $\approx$155 nm) agrees well with the value of $3.32\times10^{-18}\,cm^2$ calculated by van Dishoeck and Dalgarno [4]. An OH absorption cross-section of $\approx2\times10^{-18}\,cm^2$ at 155 nm was measured by Lee and Nee [24] using synchrotron radiation. For our UV photodissociation wavelengths around 200 nm, the $v''=2$ and $v''=3$ states show local maxima while essentially no photodissociation occurs when starting from $v''=0$.

3.2. *Molecular and Lab frame polarization of the O(^3P_J) fragment*

The O atom angular distribution can be written as

$$I(\theta) \propto 1 + \beta P_2(\cos\theta), \qquad (2)$$

where P_2 is a second-order Legendre polynomial and θ is the angle between the laser polarization vector and the recoil velocity. In the sudden recoil limit $\beta=-1$ for the perpendicular transition $1^2\Sigma^- \leftarrow X^2\Pi$. The oxygen ion image may deviate from this distribution if the O(^3P_J) atoms are polarized. The ion image angular distribution can be expanded as

$$I_J^{ion}(\theta) = p_J \sum\nolimits_{k=0,2,4} c_k(J)P_k(\cos\theta) \qquad (3)$$

where P_J are the fine-structure branching ratios. Expressions for the expansion coefficients c_k in the sudden recoil limit are given by [25]

$$\begin{aligned} c_0(J) &= 1 + \frac{1}{5}\beta\bar{\rho}_0^{(2)}(J)I_2(J), \\ c_2(J) &= \beta + \left(1+\frac{2}{7}\beta\right)\bar{\rho}_0^{(2)}(J)I, \\ c_4(J) &= \frac{18}{35}\beta\bar{\rho}_0^{(2)}(J)I_2(J), \end{aligned} \qquad (4)$$

where $\bar{\rho}_0^{(2)}(J) = \rho_0^{(2)}(J)/\rho_0^{(0)}(J)$. The rank k irreducible components of the density matrix $\rho_0^{(k)}(J)$ are related to the populations $p_{J\omega}$ of the molecule-fixed fine-structure states of the oxygen fragment, $|J\omega\rangle$, through

$$\rho_0^{(k)}(J) = \sum_{\omega=-J}^{J}(-1)^{J-\omega}\langle J,\omega,J,-\omega|k0\rangle p_{J\omega}, \qquad (5)$$

where $\langle J,\ \omega,\ J,-\omega|k0\rangle$ are Clebsch–Gordan coefficients. The relative absorption intensities $I_2(J)$ for the (2 + 1) REMPI oxygen detection scheme as defined by Mo *et al.* [26] are $I_2(1)=1/\sqrt{2}$ and $I_2(2)=-\sqrt{7/10}$ [25]. In the above equations we substituted $I_4(2)=0$.

In the sudden recoil limit the populations $P_{J\omega}$ are computed by expanding the $1^2\Sigma^-$ molecular basis $|\Lambda=0,\ S=1/2,\ \Sigma\rangle$ excited state in the product atomic basis $|S_H=\text{½}, \sigma_H|J\omega\rangle$ [25, 27]. Here Σ is the projection of the molecular spin onto the interatomic axis. Since the H atom is in an S-state, we only require the H-atom spin wave function $|S_H\sigma_H\rangle$ and the orbital part of the O(^{3}P) oxygen atom is given by $|L\Lambda\rangle$, with $L=1$ The spin part of the molecular wave function can be written as the coupling of the H-atom spin function and the O-atom spin function $|S_o\sigma_o\rangle$,

$$|S\Sigma\rangle = \sum\nolimits_{\sigma_H\sigma_O}|S_H\sigma_H\rangle|S_O\sigma_O\rangle\langle S_H\sigma_H S_O\sigma_O \mid S\Sigma\rangle, \qquad (6)$$

The uncoupled O-atom wave function may be expanded in fine-structure states through

$$|L\Lambda\rangle|S_O\sigma_O\rangle = \sum_{J=0}^{2}\sum_{\omega=-J}^{J}|J\omega\rangle\langle L\Lambda S_O\sigma_O \mid J\omega\rangle \qquad (7)$$

Combining the last two equations gives

$$\begin{aligned} |\Lambda S\Sigma\rangle = \sum\nolimits_{J\omega\sigma_H\sigma_O}&|S_H\sigma_H\rangle|J\omega\rangle\langle S_H\sigma_H S_O\sigma_O \mid S\Sigma\rangle \\ &\langle L\Lambda S_O\sigma_O \mid J\omega\rangle, \end{aligned}$$

and we find for the molecular state $1^2\Sigma^-$, with $\Lambda=0$, and $S=1/2$ and $|\Omega|=|\Sigma|=1/2$, in the sudden recoil limit

$$p_{J\omega} = \frac{1}{2}\sum_{\Omega=-1/2}^{1/2}|\langle S_H,\Omega-\omega,S_O,\omega \mid S\Omega\rangle\langle L,0,S_O \mid J\omega\rangle|^2 \qquad (9)$$

The fine-structure branching ratios for the oxygen atoms are given by $p_J=\sum_\omega p_{J\omega}$. The branching ratios for the ions, i.e. taking into account the polarization effects are given by

$$r_J = \frac{p_J c_0(J)}{\sum_J p_J c_0(J)}. \qquad (10)$$

The fine-structure populations and the Legendre moments of the normalized ion images, $\beta_J = c_2(J)/c_0(J)$

Table 1. Sudden recoil limit for the OH $X(^2\Pi)$ + h$\nu \rightarrow 1^2\Sigma^- \rightarrow$ H(^{2}S) + O(^{3}P$_J$) direct dissociation. Columns 3–5 give the populations p$J\omega$. The symbols are defined in Section 3.2.

		$\lvert\omega\rvert$						
J	P$_J$	0	1	2	$\bar{\rho}_0^{(2)}$	r_J	β_J	γ_J
0	1/9	1/9				1/8	−1	
1	1/3	0	1/6		$1/\sqrt{2}$	27/80	−5/7	−2/7
2	5/9	2/9	1/6	0	$-\sqrt{7/10}$	43/80	−25/43	−18/43

and $\gamma_J = c_4(J)/c_0(J)$ are given in Table 1. There are, for example, no projections possible of the $^2\Sigma^-$ electronic state ($\Omega = ½$) onto a final state configuration of H(^{2}S$_{½}$) and O(^{3}P$_2$) ($\Omega = 5/2,\ 3/2$). Inspection of Table 1 shows that the O(^{3}P$_{J=2:1:0}$) fine-structure branching ratios are the same as the statistical 5 : 3 : 1 pattern, but the distributions $p_{J\omega}$ for a given J value are far from statistical. The branching ratios r_J, that are obtained from integrating the angular distributions and that take into account the polarization effects, deviate slightly from the atomic branching ratios p_J. Note that the $J = 0$ O(^{3}P$_J$) product atom shows the expected $\beta = -1$ for a $\Sigma \leftarrow \Pi$ excitation, while $J = 1$ and 2 have $\beta > -1$ and significant (negative) γ values.

4. Experimental method

The velocity map imaging apparatus has been described in detail elsewhere [1, 16], thus only a summary of the experimental details concerning the molecular beam and hexapole state selector will be given here. Two differentially pumped vacuum chambers are used: one chamber for the production of OH/OD molecules and the other chamber for the state selection of OH/OD photodissociation, and detection of one of the fragments from OH/OD. The source chamber is pumped by a diffusion pump and the detection chamber is differentially pumped by a turbo pump with additional pumping by a liquid N_2-cold trap. The OH/OD beam source was produced by a mixture of H_2O/D_2O molecules seeded in Ar as the carrier gas. The mixture is prepared by bubbling Argon at a backing pressure of 1.5 bar through liquid water at room temperature (vapour pressure of 24 mbar). For the expansion a Jordan pulsed valve with a 0.4 mm diameter nozzle is used, which is mounted along the direction of the time of flight tube. The OH/OD radicals are produced by dissociation of H_2O/D_2O at the beginning of the expansion by an electrical discharge between a stainless steel ring (4 mm diameter, 0.5 mm thick) and the grounded valve body [7]. The ring, which is located on-axis 2.5 mm from the nozzle, is pulsed (20 µs, −2 kV) to negative high voltage during the ≈60 µs expansion.

After their production, the electrically neutral OH/OD molecules cool down to the ground rotational level of each vibrational state in the supersonic expansion and pass through a 1 mm diameter skimmer which separates the source and detection chambers. The skimmer is positioned 15 mm from the nozzle. The cold molecular beam enters a 120 mm long hexapole state selector 50 mm downstream of the nozzle, which focuses OH/OD in the $\Omega = 3/2$, $J = 3/2$, $|M_J| = 3/2,\ 1/2$ states in the upper Λ-doublet of f-symmetry [28] to the laser interaction region between the repeller plate and the extractor plate of the electrostatic lens. The hexapole is constructed with 3 mm cylindrical rods and has an inner diameter of 6 mm. The distance from the entrance of the hexapole to the valve and the distance from the exit of the hexapole to the collision center is 50 mm. The total distance between the valve and the collision zone is 220 mm. The enlargement of the distance between the source and photodissociation area by the insertion of the state selector decreases the contributions from all other species in the discharge beam, while the hexapole increases the concentration of the state-selected component by a factor of ≈8 at the crossing point with the photodissociation laser.

Using both laser induced fluorescence (LIF) and resonance enhanced multiphoton ionization (REMPI) detection techniques [29, 30] the only species in the beam that was found to focus with the hexapole was OH/OD. A corresponding increase in signal for the photodissociation processes with the hexapole 'on' is thus direct proof that the photodissociation signal arises from OH/OD. The UV laser beam propagates perpendicular to the molecular beam and is focused with a 200 mm focal length lens, and has its electric field polarization direction lying parallel to the detector face. In our experiments only one laser is used, both for dissociation of the OH/OD and detection of one of the fragments O(^{3}P$_{2,1,0}$) from OH, O(^{3}P$_{2,1,0}$) from OD or D(^{2}S) from OD. There was too

much apparatus background to detect H from OH. The laser wavelength is chosen for two-photon resonant three-photon ionization [(2 + 1) REMPI] of either the O($^3P_{2,1,0}$) atom products at ≈226 nm and ≈200 nm [31] or the D(^2S) atom products at ≈243 nm and ≈205 nm. We find that the relative sensitivity for all three O(^3P_J) states at ≈200 nm is similar and that the overall sensitivity is a factor of ≈ 7 lower than at ≈226 nm for similar experimental conditions.

UV laser light of ≈2mJ/pulse was generated by frequency doubling the output of a dye laser (Continuum TDL60) for ≈226 nm (Coumarin 47 dye) and ≈243 nm (Coumarin 102 dye). In the 200–205 nm region ≈1 mJ/pulse was generated by frequency tripling the output of a dye laser (Spectra Physics Quanta Ray PDL-2) operating with a mixture of Sulforhodamine B and Rhodamine 640. Ions created in the laser-molecular beam intersection area are extracted and rapidly accelerated into the time-of-flight region by an electrostatic velocity mapping lens consisting of a 100 mm diameter repeller, extractor, and ground plates separated by 15 mm. The repeller electrode has a 4 mm centre opening and the other two lenses have openings of 20 mm. At the end of the TOF tube the ions strike a position sensitive detector, which consists of two microchannel plates (MCP) followed by a P-20 phosphor screen. Mass selectivity was achieved by pulsing on the gain of the detector as the D^+ or O^+ ions arrive. The 2-D images on the phosphor screen are recorded with a CCD camera and stored in a PC where further data analysis is performed.

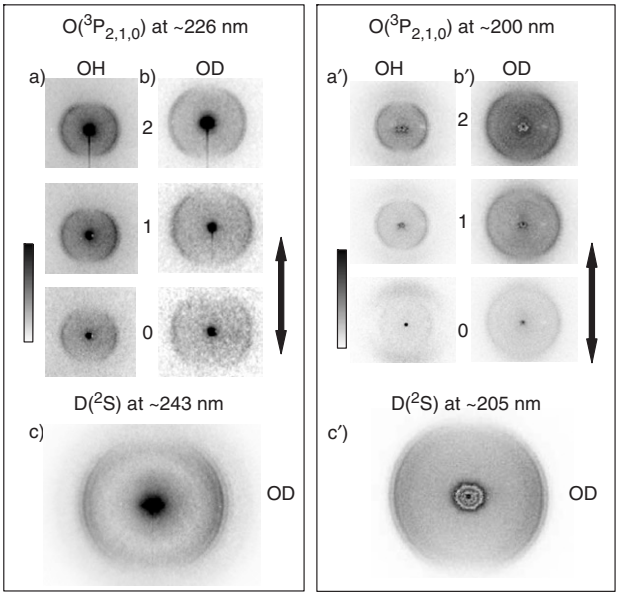

Figure 2. Raw O^+ images produced by one-photon photodissociation of: (a) OH and (b) OD. The O(2p ^3P_J) ($J = 2, 1, 0$) atoms were ionized by (2 + 1) REMPI through the O(3p ^3P_J) states (images a) and b)) at ~226 nm, and by (2 + 1) REMPI through the O(4p ^3P_J) states (images a′) and b′)) at ~200 nm. Raw images of D^+ from the one photon dissociation of OD formed from D(1s ^2S) atoms by (2 + 1) REMPI through the: (c) D(2s ^2S) state at the wavelength 243.09 nm and (c′) D(3s ^2S) states at 205.07 nm. A grayscale bar (left side) shows the relative signal intensity, where the darker areas correspond to higher signal. The dot in the centre of each image corresponds to zero-velocity fragment O(^3P_J) or D(^2S) atoms formed in the discharge source. The outer rings originate from photodissociation of vibrationally excited OH/OD $X\,^2\Pi$ radicals. The vertical arrow indicates the direction of the laser polarization.

5. Experimental results and analysis

5.1. *General description of the images*

A set of raw photofragment images of O(^3P_J) photofragments from the photo-dissociation of OH and OD, and D(^2S) photofragments from the photodissociation of OD are shown in Figure 2. These images are 2D projections of the 3D velocity distributions with the polarization vector of the photodissociation laser beam maintained parallel to the detector face and thus along the vertical axis of the figure. All of the images show a strong spot in the middle of the image which corresponds to O(^3P_J) or D(^2S) atoms formed in the discharge and cooled in the expansion.

State-selective detection of O($2p^4\ ^3P_J$) is achieved either by two-photon resonant, one-photon ionization ((2 + 1) REMPI) through the O($2p^3 3p^1$, ^3P_J) states using the vacuum wavelengths of 225.654, 226.059 and 226.233 nm for $J = 2$, 1, 0, respectively or by (2 + 1) REMPI through the O ($2p^3 4p^1$, ^3P_J) states using the vacuum wavelengths of 200.640, 200.959 and 201.097 nm for $J = 2$, 1, 0, respectively. State-selective detection of D (1s ^2S) is achieved either by (2 + 1) REMPI through the D(2s ^2S) state using the vacuum wavelengths 243.09 nm or by (2 + 1) REMPI through the D(3s ^2S) states using 205.07 nm. The images shown in Figure 2 are calibrated using O($^3P_2$) from the photodissociation of O_2 at ~226 nm and by D(^2S) from DI photodissociation at ≈243 nm. The radius of the ring is proportional to the velocity of the products, so after calibration at one radius the kinetic energy release corresponding to all other rings is determined. At least two rings are seen in each image in Figure 2, each with a perpendicular (≈$\sin^2\theta$, with $\theta = 0^\circ$ defined at the top centre axis of the image) angular distribution. An overview of the velocity information extracted for each observed ring is presented in Table 2. As required from momentum balance, the O images from OD photodissociation are larger (in the proper ratio) than those from OH photodissociation at the same energy, which is an additional proof that the images originate from OH/OD.

Table 2. Experimentally observed and calculated fragment recoil velocity, velocity uncertainty, kinetic energy and ion-recoil velocity for photodissociation of OH and OD at 243, 226, 205, and 200 nm.

Parent	Frag.	λ_{diss} (nm)	Assign.	TKER (eV)	$v_{calc.}$ (m/s)	$v_{meas.}$ (m/s)	Δv (m/s)	Spacing (m/s)	v_{recoil} (m/s)
OH	$O(^3P_J)$	226	$v''=2$	2.02	1173	1200	20	117	35
			$v''=3$	2.39	1290	1300			
OD	$O(^3P_J)$	226	$v''=3$	2.08	1622	1670	35	118	35
			$v''=4$	2.32	1740	1765			
OH	$O(^3P_J)$	200	$v''=1$	2.23	1252	1250	20	115	45
			$v''=2$	2.60	1367	1345		98	
			$v''=3$	3.08	1465	1475			
OD	$O(^3P_J)$	200	$v''=2$	2.34	1774	1770	20	109	45
			$v''=3$	2.64	1883	1870		103	
			$v''=4$	2.98	1986	1995			
OD	$D(^2S)$	243	$v''=2$	1.33	10420	10680	220	1185	212
			$v''=3$	1.56	11605	11555		1040	
			$v''=4$	1.80	12650	12430			
OD	$D(^2S)$	205	$v''=1$	1.80	12745	12425	230	920	347
			$v''=2$	2.16	13765	13610		835	
			$v''=3$	2.44	14685	14470			

Raw (hexapole on-off) $O(^3P_J)^+$ images produced by photodissociation of OH and OD at ≈226 nm are presented in Figure 2a and b, respectively, and a raw $D(^2S)^+$ image (hexapole on-hexapole off) produced by photodissociation of OD at ≈243 nm is presented in Figure 2(c). All of these images are summations of 50000 laser shots. The background-induced signal at the center of the images is not fully eliminated by the hexapole on-off subtraction scheme, causing a slight overload of the CCD camera at this position, especially for the $O(^3P_2)$ images. Raw $O(^3P_J)$ images for photodissociation of OH and OD at ~200 nm which are taken using event counting and only with the hexapole 'on' are shown in Figure 2(a′) and (b′), respectively. In Figure 2(c′) a raw (hexapole on-hexapole off) $D(^2S)^+$ image produced by photodissociation of OD at ≈205 nm is presented. The O^+ images from OH are summations of 90 000 laser shots, and the O^+ and D^+ images from OD are summations of 230 000 laser shots.

Direct detection of $O(^1D_2)$ products from the dissociation of OD using (2 + 1) REMPI via the $^1P_1$ state at 205.473 nm (vac.) was also attempted. While a small signal at the centre of the image from $O(^1D)$ produced in the discharge was observed, we did not observe any convincing $O(^1D)$ signal from the photodissociation of OD at 205 nm.

5.2. *$O(^3P_J)$ branching ratios*

Experimental branching ratios for the channels [O ($^3P_2$) + H (^2S)]: [O ($^3P_1$) + H (^2S)]: [O ($^3P_0$) + H (^2S)] of OH and [O ($^3P_2$) + D (^2S)]: [O ($^3P_1$) + D (^2S)]: [O ($^3P_0$) + D (^2S)] of OD at ≈226 and ≈200 nm are given in Table 3. The total OH photodissociation signal strength was determined for each raw image at constant laser pulse energy. For these one-laser experiments, the dissociation and detection laser polarization are the same, and set parallel to the imaging detector plane. No corrections were made for the effects of the fixed (linear) laser polarization on the total detection sensitivity. A simulation of the experiment using the sudden-limit values from Section 3 predicts a < 5% deviation between a polarized and non-polarized detection laser, which is less than our experimental uncertainty.

Table 3. Experimentally observed $O(^3P_J)$, $(J = 2, 1, 0)$ branching ratios (uncertainty 0.05) from the photodissociation of OH and OD at 226 and 200 nm.

		Branching ratio		
		$J=2$	$J=1$	$J=0$
~226 nm	OH	0.59	0.30	0.11
	OD	0.51	0.35	0.14
~200 nm	OH	0.55	0.33	0.13
	OD	0.49	0.35	0.16

5.3. *Velocity and kinetic energy analysis and assignment of the images*

Velocity and kinetic energy data is presented in Table 2. The two main rings seen in the $O(^3P_J)$ images

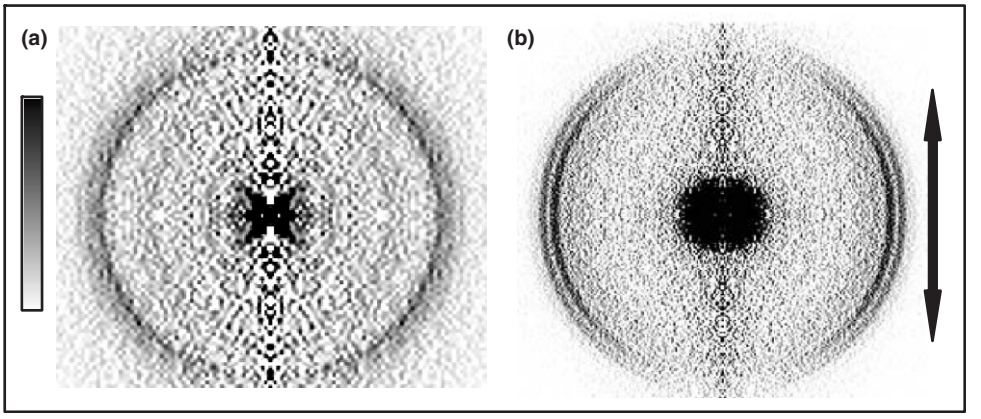

Figure 3. Abel inverted images of: (a) $O(^3P_2)$, (b) $D(^2S)$ formed from the one photon dissociation of vibrationally excited OD $X\ ^2\Pi$ radicals at ≈200 and ≈205 nm, respectively. On the left side a intensity grey-scale is presented. On the right side the vertical arrow presenting the laser polarization. The $O(^3P)$ image is smaller than the D image, it has been scaled to the same size for comparison. Note that the weak extra inner rings in the O (^3P) images for OD come from an OH impurity.

(Figure 2(a)) arising from photodissociation of OH at ≈226 nm, for example, have a velocity of 1200 and 1300 m/s, respectively, with an uncertainty in the peak position (Δv) of +/−20 m/s. Converting these velocities to total kinetic energy release [$TKER = (m_{OH}/m_H) \times KER_O$ ($= m_O v_O^2$)] yields values of 2.02 and 2.39 +/−0.06 eV, respectively. TKER for O atoms from OD photodissociation $= (m_{OD}/m_D) \times KER_O$ and for D atoms from OD $TKER = (m_{OD}/m_O)KER_D$.

Kinetic energy distributions were obtained from the inversion of raw images using the BASEX program [32], which assumes cylindrical symmetry about the dissociation laser polarization in the experiment. Possible deviations from cylindrical symmetry due to the state-selection of the molecular beam are discussed in section 5.8. The effects of product atom alignment were accounted for in the theoretical analysis of Section 3. Vertical sections through the 3-D distribution of two representative inverted images of O ($^3P_2$) and D (^2S) from the photodissociation of OD at 200 and 205 nm, respectively are shown in Figure 3(a) and (b).

The corresponding kinetic energy distributions from these reconstructed images, extracted by integrating over all angles, are shown in Figure 4. Weak signals due to OH are seen at lower kinetic energy in the $O(^3P_2)$ from OD image. The reconstructed images from $O(^3P_2)$ REMPI at ~226 and ~200 nm arising from the photodissociation of OH are shown in Figure 5, and the corresponding TKER curves obtained from integrating over the angular distribution of the inverted images are shown in Figure 6. A beam vibrational temperature is estimated from the relative peaks heights in the kinetic energy distributions.

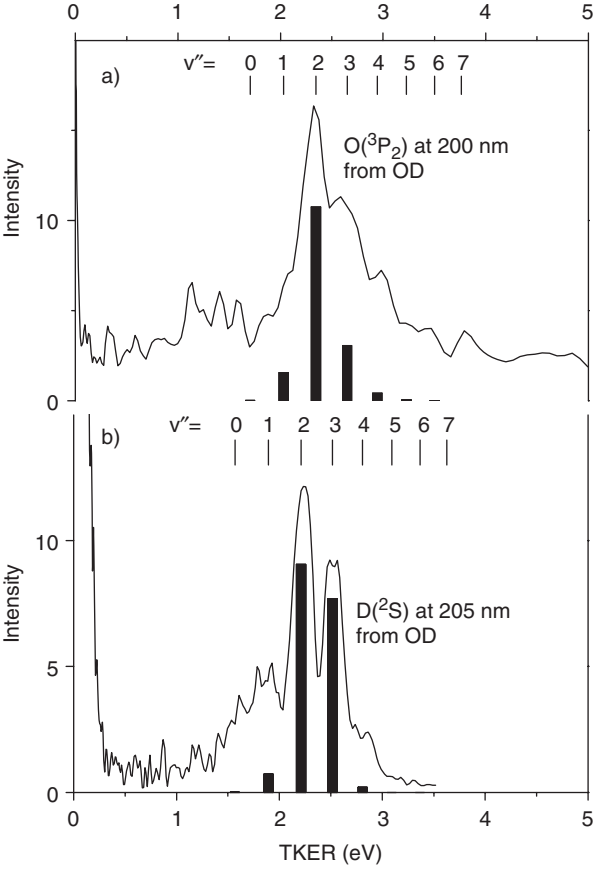

Figure 4. Total kinetic energy release (TKER) distribution for the images shown in Figure 3. The initial vibrational state of OD is determined from energy balance with $TKER = h\nu + E(vib)_{OD} - D_0(OD)$. The bar graphs show the calculated photodissociation yields for OD $X\ ^2\Pi$ (v'') at a vibrational temperature of 2000 K.

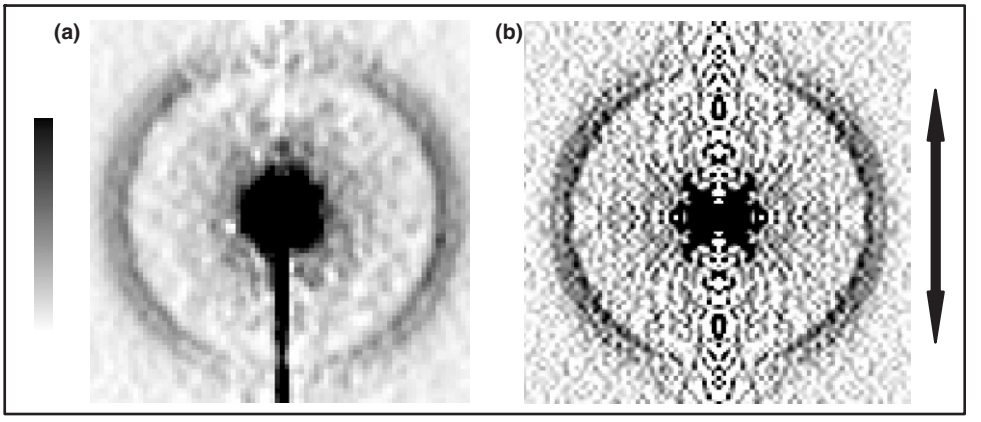

Figure 5. Abel inverted images of $O(^3P_2)$ formed from the one-photon dissociation of vibrationally excited OH $X\,^2\Pi$ radicals at: (a) ≈226 and (b) ≈200 nm, respectively (rescaled to same size). See Figure 2 caption for other details.

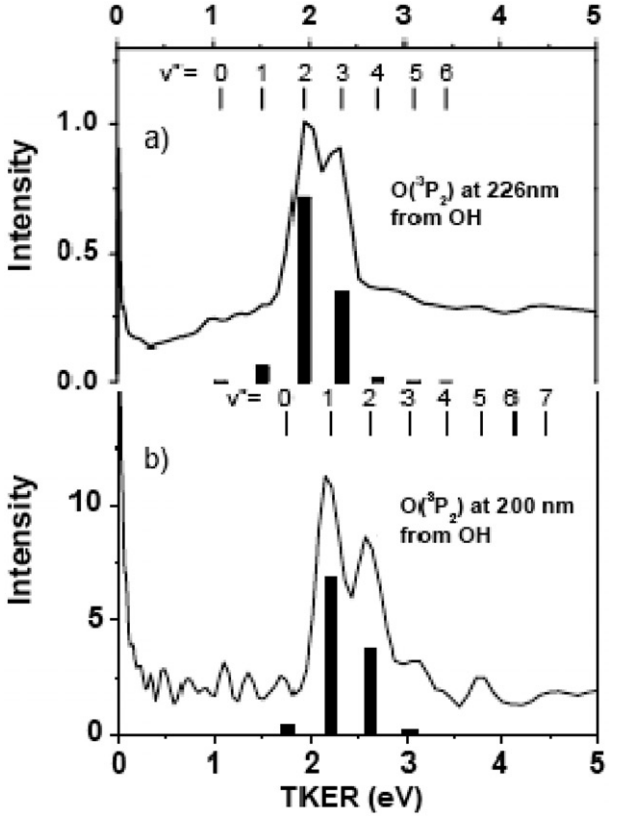

Figure 6. Total kinetic energy release (TKER) distribution for the images shown in Figure 5. The initial vibrational state of OH is determined from energy balance with $TKER = h\nu + E(vib)_{OH} - D_0(OH)$. The bar graphs show the calculated photodissociation yields for OH $X\,^2\Pi$ (v'') at a vibrational temperature of 2000 K.

Each peak in the kinetic energy distribution can be assigned using the energy balance equation $TKER = h\nu + E(vib)_{OH/D} - D_0(OH/OD)$, with the bond energy of OH/OD, $D_0(OH/OD)$, from [3, 33, and 34], and the recently calculated vibrational energies for ground $X^2\Pi$ state of OH/OD, $E(vib)_{OH/D}$, from Loo and Groenenboom [9]. Complementary first principle calculations (Figure 1) confirm that one-photon excitation of OH/OD $X^2\Pi(v'')$ to the repulsive $1\,^2\Sigma^-$ curve has a reasonably strong ($\sigma_{max} > 10^{-20}\,cm^2$), wavelength-dependent photodissociation cross-section in the 200–250 nm region. The two main rings seen for O (^3P_J) atom detection at 226 nm in Figure 2(a), for example, attributed in Table 2 to photodissociation of OH in vibrational levels $v'' = 2$, and 3, have photodissociation cross-sections of $\approx 6.45 \times 10^{-20}\,cm^2$ and $\approx 3.22 \times 10^{-19}\,cm^2$, respectively. Depending on the dissociation/detection wavelength and the molecule (OH or OD), excitation of the OH $X(v'')$ $v'' = 1$–4 states are observed. We should point out that the vibrational energy of OH($v'' = 3$) is $10199.39\,cm^{-1}$, which for a molecular beam temperature of ≈2000 K (see next section) has a population probability of only 2×10^{-5}.

5.4. *Temperature of the discharge beam*

The relative intensity of the peaks observed in the TKER curves of Figures 3 and 5 can be qualitatively understood using the photodissociation cross-sections computed for each OH $X(v'')$ vibrational state (Figure 1). The relative peaks heights determined from the O ($^3P_2$) and D (^2S) fragment atoms images for the higher energy regime, ≈200 and ≈205 nm, respectively, were found to agree with calculated photodissociation yields for an OD molecular beam with a vibrational temperature of 2000 K. While in our previous study [1], a vibrational temperature of ≈1700 K was estimated, a vibrational temperature of 2000 K agrees better with the present, more extensive, experimental data. The effect of an electric discharge

on the vibrational excitation, relaxation, and energy transfer of diatomic molecules in pulsed supersonic beams has been the subject of several previous studies [35–38]. The final vibrational temperature of a pulsed discharge has been found to depend on a large number of experimental parameters, including backing pressure, buffer gas, discharge condition and geometry of the nozzle. Our experimental value compares reasonably with other studies of discharge sources. A discharge of NO in He produced an NO vibrational temperature of 6500K, for example [37], while a similar discharge [38] in OCS produced an SO vibrational temperature of ≈1000 K.

At a vibrational temperature of 2000 K, the $v''=$ 1–3 states of OH contains only 5, 0.3, and 0.002% of the total population. The sensitivity of the imaging experiment is thus quite high in order to image the neutral photodissociation products from such small fractions of the beam population. In our previous 2 + 1 REMPI study [16] of OH we were able to detect transitions from the ($v''=1$, 2, 3) vibrational ly excited states to the higher lying $D^2\Sigma^-$ and 3 $^2\Sigma^-$ Rydberg states. We did not observe any (2 + 1) REMPI transitions from vibrational levels higher than $v''=3$. A previous study used the same OH source as in the present study and the REMPI spectra also confirmed that the OH radicals produced in the discharge source are indeed vibrationally hot, but rotationally quite cold (< 20 K). The population in the excited rotational states is effectively relaxed in the supersonic expansion due to the relatively small rotational spacing but the vibrational spacing is too large to allow an efficient relaxation.

5.5. *Ion recoil effects on kinetic energy resolution*

While ion recoil [39–41] is deleterious in both O atom and D atom imaging, the O atom kinetic energy resolution is most affected, as is evident in the curves shown in Figure 4. Photodissociation of a state-selected diatomic molecule should lead to sharp peaks in the KER curves, while the observed peaks are quite broad. In our previous OH photodissociation study [1] we pointed out that the velocity resolution is limited by ion recoil from the (2 + 1) REMPI detection process. The large excess ionization energy (3 hν-IP) when partitioned by momentum conservation creates a high velocity electron and low, but non-zero, velocity fragment ion. This effect is most important for combined photodissociation and REMPI detection using the higher energy ≈200 and ≈205 nm photons. On conversion of the neutral fragments to ions, the ion recoil, a fixed and known velocity sphere, is added to the original velocity vector of the neutral O(^3P_J) and D(^2S) photofragments. While the added ion-recoil velocity is relatively small, it causes significant broadening when its magnitude approaches the velocity spacing of neighbouring rings in the image. The percentage effect of ion recoil on the velocity of the nascent O or D fragment is roughly independent of the fragment mass because a higher mass atom (O from OH/OD) has a lower nascent velocity due to the mass partitioning factor in the TKER equation.

In order to quantify the O atom ion recoil we have measured an O^+ image of cold (zero transverse velocity) O($^3P_2$) atoms created in the discharge beam. A magnification lens similar to that of reference 42 was used to magnify the image of low velocity O^+ to observe the ion-recoil effect. O($^3P_2$) ion-recoil is characterized as a mixed perpendicular angular distribution ($\beta\sim-0.2$), which causes significant broadening of the O/D atom signal, especially along $\theta=90^\circ$, where θ is the angle between the recoil velocity vector and the polarization direction of the linearly polarized REMPI laser. This anisotropic broadening is added to each velocity component of the perpendicular ($\Sigma\leftarrow\Pi$) angular distribution.

The two-photon excited $n=2s$ electron in the (2+1) REMPI of D(^2S) atoms at ≈243 and ≈205 nm is ejected as a p wave, thus with a pure parallel or $\cos^2\theta$ distribution. This causes an observable splitting of the rings in the regions of from $0 < \theta < 45^\circ$ and blurring of the rings around $\theta=90^\circ$, where most of the signal lies. It is possible to decrease the recoil blurring by using slicing methods [43] and by setting the probe laser polarization direction perpendicular to the detector face.

The ion recoil velocity (Table 2) for O and D atom detection at the employed wavelengths should be compared with the photofragment velocity. In the case of (2+1) REMPI of O(^3P_J) atoms at ≈226 nm, for example, the three-photon energy is 16.47 eV while the O atom ionization potential is 13.62 eV. The total excess kinetic energy is 2.9 eV, which is subdivided between the electron and O^+ ion according to the mass ratios, i.e. $\mathrm{KER}(O^+)=(m_e/m_o)\times\mathrm{TKER}$ ($m_e=5.5*10^{-4}$ amu), yielding $v_{\mathrm{recoil\ O+}}=35$ m/s. The shifts in velocity for the rings observed in this study vary over the range of ±1.7% to ±3.6%. More important is the relative peak spacing of the rings compared to the ion recoil. Since the recoil adds in all directions, photodissociation of the OH $v''=2$ and 3 molecules at 226 nm, for example, yields O atom peaks along $\theta=90^\circ$ that are shifted closer to each other by 70 m/s, compared to their original spacing of 118 m/s. Other apparatus effects, particularly space charge and

the transverse velocity spread of the parent OH beam, produce further broadening of the peaks.

5.6. *Angular distributions*

Angular distributions, $I(\theta)$, were obtained by integrating the inverted image over the velocity range (which includes the ion-recoil spreading) of each ring. These are fitted to the expression: $I(\theta) \sim 1 + \beta P_2(\cos\theta) + \gamma P_4(\cos\theta)$ where $P_2(\cos\theta)$ and $P_4(\cos\theta)$ are the second- and fourth-order Legendre polynomials, respectively, and β and γ are anisotropy parameters. In the absence of alignment in the probed fragment, the anisotropy parameter β ($-1 \le \beta \le +2$) is -1 for a pure perpendicular transition and $+2$ for a pure parallel transition. These extreme values of β can only be obtained if the dissociation lifetime τ of the excited state is much shorter than the rotation period, τ_{rot}, of the parent molecule (direct axial dissociation). In the absence of product atom alignment (O^3P_0 and D^2S products) the anisotropy parameter $\gamma = 0$. When atomic alignment is present and probed by the linearly polarized REMPI laser, both β and γ are necessary to fit the angular distributions, as is described in the sudden limit analysis.

A perpendicular transition from the ground $X^2\Pi$ state to the directly dissociative $1^2\Sigma^-$ electronic state should yield $\beta = -1$. As is obvious from Figure 2, all of the observed angular distributions are roughly perpendicular. For the stronger rings in the D(^{2}S) atom images for photodissociation of OD at ≈243 and also at ≈205 nm, an almost fully perpendicular angular distribution is observed. As discussed in the next section, a fully perpendicular angular distribution ($\beta = -1$) for photodissociation of OD at ≈243 nm was measured for the strongest ring in the D^+ image by applying Doppler-free (2+1) REMPI, which is less sensitive to background D atoms than standard (2+1) REMPI.

Representative angular distributions for the strongest peaks of the dissociation products O(^{3}P$_{2,1,0}$) from OH/OD at 226 and 200 nm and D (^{2}S) from OD at 243 and 205 nm are shown in Figure 7. Anisotropy parameters β, γ determined from the angular distribution of O(^{3}P) fragments are given in Table 4. The estimated uncertainty of β and γ is typically 0.1. Uncertainty values of β or γ exceeding 0.1 are indicated in the table. It is clear from Table 4 that the fine-structure dependent β parameters at 226 and 200 nm deviate strongly from -1 for O(^{3}P$_{2,1}$). Alignment of the O(^{3}P$_{2,1}$) photofragments is observed as a dip in signal strength (corresponding to a negative γ value) along the $\theta = 90^\circ$ in the image. β becomes more negative as the angular momentum J of the O(^{3}P$_J$) photofragments decreased and the value of the anisotropy parameter γ increases with the decreasing values of β over the fine structure levels. These trends are predicted by the sudden limit analysis in Section 3.

In Figure 8 the anisotropy parameters β and γ from Table 4 are plotted as a function of dissociation wavelength. It can be seen from this figure that the anisotropy parameters of the three O(^{3}P$_J$) channels are different from each other, but there are no large variations in these parameters (within the experimental error limit) as a function of excitation energy at ≈226 and ≈200 nm. There is also no significant variation in the β parameter for D atoms from OD photodissociation at 243 nm compared to 205 nm.

5.7. *Doppler-free imaging*

Another origin of ring broadening is space charge, which occurs when the laser-created ion density is too large. On increasing the laser power as much as possible to obtain a reasonable photofragment signal we also ionize non-signal species which further increases space charge. To decrease this effect and also avoid errors in scanning over the Doppler profile when taking the image, we apply the Doppler-free (2+1) REMPI [44] to probe the D atom products from photodissociation of OD. In our configuration we used two counter-propagating linearly polarized laser beams to ionize the D(1s ^2S) atoms by (2+1) REMPI through the D(2s ^2S) state at the center wavelength of 243.09 nm. The laser light at 243.09 nm (≈1.5 mJ/pulse, 5 ns pulse length, 0.4 cm^{-1} bandwidth) is tuned to the centre of the Doppler profile and focused with a 20 cm lens onto the molecular beam. The laser beam was retro-reflected with a 25 cm focal length spherical mirror and refocused onto the molecular beam. The polarization vector of the both beams was parallel to the detector face. Note that this configuration is not optimal, there is a 50 cm (≈2 ns) delay between the two beams, and the laser bandwidth is also much broader than desired for optimal Doppler-free detection. When the two beams overlap spatially the total signal increased by a factor of ≈15, which allowed the use of lower laser power and thus resulted in less space charge and background effects. The Doppler-free condition ensures detection of all velocity components with equal sensitivity, but the two single-beam signals which are always present strongly favour detection of the zero velocity atoms from the discharge, which appear in the centre of the image. The D atom Doppler-free signal is not disturbed by the zero velocity signals in the middle of the image.

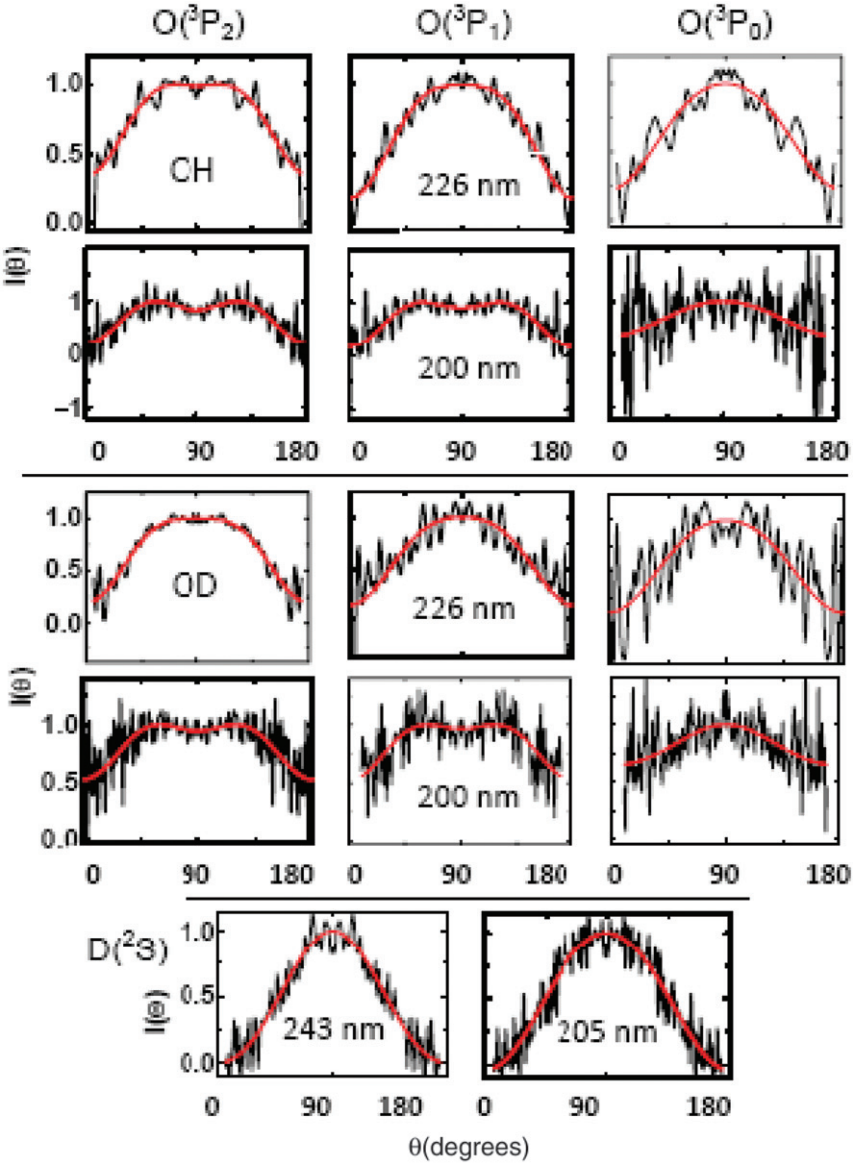

Figure 7. The measured angular distribution and fitted curves for the strongest peaks of the dissociation products O ($^3P_{2,1,0}$) coming from one-photon dissociation of: (a) OH at ≈226 (upper panel) and ≈200 nm (lower panel); (b) OD at ≈226 (upper panel) and ≈200 nm (lower panel); and (c) measured angular distribution and fitted curves for the strongest peaks of the dissociation products D (2S) coming from one-photon dissociation of OD at ≈243 and ≈205 nm, respectively. The angular distribution is fit to the expression: $I(\theta) = 1 + \beta P_2(\cos\theta) + \gamma P_4(\cos\theta)$.

The Doppler free raw image of D(^{2}S) and the corresponding slice through the inverted 3-D image are presented in Figure 9. By this method a pure perpendicular angular distribution was measured for the strongest ring in D atom image ($\beta = -1.0 \pm 0.1$)

5.8. *Effect of parent molecule orientation and alignment*

Our experimental conditions, i.e. a molecular beam passing through a hexapole state selector into a static electric field, are similar to those used for studies of the photodissociation of oriented OCS molecules [45] or orientation effects in OH inelastic collisions [46]. On exiting the hexapole the *f*-state selected OH molecules ($\Omega = 3/2$, $J = 3/2$, $M_J = 3/2, 1/2$) fly 5 cm before passing through a 4 mm hole in the center of the repeller plate electrode, which is biased typically at −3000 V. Due to this large repeller plate opening and single hexapole configuration we estimate that at about 60% of the OH molecules studied are in the $M_J = 1/2$ state. Within the imaging lens, at the point where photodissociation

Table 4. (Top) Experimentally determined anisotropy parameters β_{exp} and γ_{exp} extracted for the strongest peaks seen in the background subtracted and fine structure state selected O^+ images for one-photon dissociation of OH/OD at ≈226 and ≈200 nm. (Middle) the corresponding anisotropy parameters β_{calc} and γ_{calc} predicted theoretically, using the sudden limit analysis. (Lower) Experimentally determined anisotropy parameters β_{exp} extracted for the strongest peaks seen in the observed background subtracted D^+ images coming from one-photon photodissociation of OD at ≈243 and ≈205 nm and anisotropy parameters β extracted for the strongest peaks seen in the Doppler-free D^+ image from one-photon photodissociation of OD at ≈243 nm. The estimated uncertainty of β and γ is 0.1. Values of the uncertainties in β and γ which are larger than 0.1 are indicated in the table.

		$O(^3P_2)$		$O(^3P_1)$		$O(^3P_0)$	
Transition		β_{exp}	γ_{exp}	β_{exp}	γ_{exp}	β_{exp}	γ_{exp}
~226 nm	OH ($v''=2$)	−0.44	−0.23	−0.74	−0.10	−0.86	+0.08
	OD ($v''=3$)	−0.56	−0.20	−0.64	+0.03	−0.82	−0.05
~200 nm	OH ($v''=1$)	−0.52	−0.43(15)	−0.65	−0.31(19)	−0.94(51)	−0.96(70)
	OD ($v''=2$)	−0.61(16)	−0.27(22)	−0.67(18)	−0.09(23)	−0.99(65)	+0.26(87)

		$O(^3P_2)$		$O(^3P_1)$		$O(^3P_0)$	
		β_{calc}	γ_{calc}	β_{calc}	γ_{calc}	β_{calc}	γ_{calc}
Sudden limit analysis		−0.58	−0.42	−0.71	−0.28	−1	0

			$D(^2S)$
~243 nm	OD ($v''=3$)	β_{exp}	−1.06
		β	−1.02
~205 nm	OD ($v''=2$)	β_{exp}	−1.00

and photoionization takes place, the static field is ≈710 V/cm. While this is a rather low field, it causes parity mixing of the e and f levels and a slight pre-orientation of the state-selected OH [46]. Parity mixing is observable in the REMPI and LIF spectra of the state-selected OH, and can be avoided by pulsing on the velocity mapping field after laser excitation and ionization has taken place. Pre-orientation of the M_J=1/2 state is negligible at 710 V/cm, and pre-orientation of the $M_J = 3/2$ state caused by this field is not observable in a photodissociation process because the orientation field is parallel with the ion TOF direction. Information mapped along the TOF direction is lost in the 'crush' of the 3D image onto the 2D detector. Our OH sample used for photodissociation imaging is thus effectively isotropic within our data uncertainties, which means we can assume cylindrical symmetry around the laser polarization direction in order to analyse the raw images using standard inversion procedures (Basex program) [32].

6. Discussion

Experimentally observed $O(^3P_J)$ fine structure branching ratios and angular distribution parameters (β, γ for OH/OD photodissociation in the UV region are presented in Tables 3 and 4 respectively, and the angular distribution data is plotted in Figure 8 along with the calculated sudden-limit values given in Table 1. Within the error limits of the experiment, both the branching ratios and polarization sensitive angular distribution parameters agree with the calculated sudden-limit values for OH and OD at each dissociation wavelength.

The sudden-limit analysis of Section 3 assumes a single state (the $1\,^2\Sigma^-$ state) is optically prepared in the Franck-Condon region of the OH molecule. Lee [15] has argued that in the high-energy region between the first and second dissociation thresholds of OH that predissociative levels of the $A\,^2\Sigma^-$ ($v' \geq 7$) state can also be accessed from the $v''=0$ level of the ground state, and interference from the predissociative and direct dissociation pathways could cause a strong local variation in the $O(^3P_J)$ fine structure branching ratios. By tuning the dissociation laser wavelength, the desired $O(^3P_J)$ product atom can then be selected in a type of internal coherent control method. In our experiment excitation takes place from OH $X(N''=1,\ J''=3/2,\ v''=0$–$5)$ at the dissociation wavelengths 243, 226, 205, and 200 nm. A number of $A\,^2\Sigma^-$ ($v' \geq 7$) states lie in the 243–200 nm region when starting from X ($v''=0$–4), but none are close to resonance with

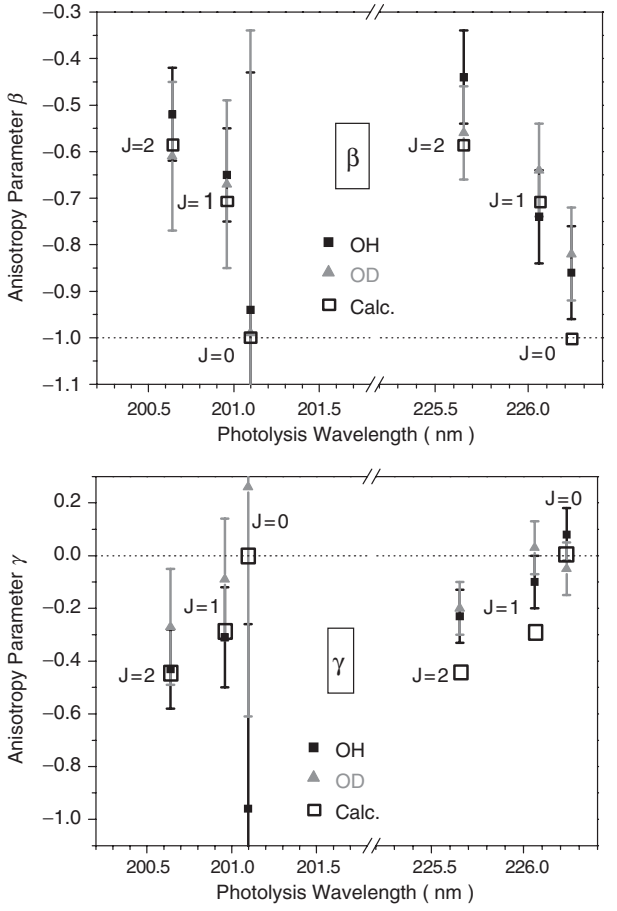

Figure 8. Experimental β and γ values plotted as a function of wavelength ($\approx$226 and $\approx$200 nm) corresponding to the different fine structure states of the $O(^3P_J)$ atom ($J=2,1,0$) from photodissociation of OH and OD. β and γ with experimental error bars are represented by a filled square for OH and by a filled triangle for OD. Calculated anisotropy parameters β and γ in the sudden-recoil limit, characterizing the angular distribution of $O(^3P_J)$ (with $J=2,1,0$) photofragments formed in the one photon process photodissociation of OH/OD via the $1\,^2\Sigma^-$ state are represented by a hollow square.

the specific O, H, or D atom REMPI lines we employ. Excitation beginning from higher vibrational levels of the X state probes progressively larger internuclear distances, which favors excitation to the repulsive $1\,^2\Sigma^-$ state over excitation to bound levels of the $A\,^2\Sigma^-$ state. To produce the predicted branching ratio variations, the contributions from the two indistinguishable dissociation pathways should be roughly comparable. We believe that excitation to bound levels of the $A^2\Sigma^-$ state is extremely weak at our photodissociation wavelengths so that the photodissociation dynamics is reduced to that on the single $1\,^2\Sigma^-$ state. Zhou *et al.* [10] come to a similar conclusion in an investigation of the photodissociation dynamics of the isovalent SH molecule.

Lee also found that at energies above the second dissociation limit producing $H(^2S)+O(^1D)$, the nonadiabatic (spin-orbit and Coriolis) couplings among electronic states correlating to $O(^3P)$ are very small compared with the kinetic energies of the $O(^3P)$ fragments, and because of that their effects on the dissociation to $O(^3P)$ are expected to be minimal [47]. Lee found that the anisotropy parameters for $O(^3P_J)$ produced by photodissociation above the second dissociation limit are nearly energy-independent, and very close to -1, and that the $O(^3P_J)$ fine structure branching ratios are also very similar to the recoil limit values in this energy regime.

Zhou *et al.* [10] studied the photodissociation dynamics of jet-cooled SH in the photolysis wavelength region of 216 to 232 nm using the high-n Rydberg atom time of flight technique. Their results also indicate that UV photolysis of SH is due to one- photon direct dissociation of SH to the dissociative $1\,^2\Sigma^-$ curve from the ground state of SH ($X^2\Pi$, $v''=0$–2). Their product fine structure states distributions also showed that the $S(^3P_J)$ spin–orbit branching fractions of SH are close to the 5 : 3 : 1 sudden limit distribution from the single

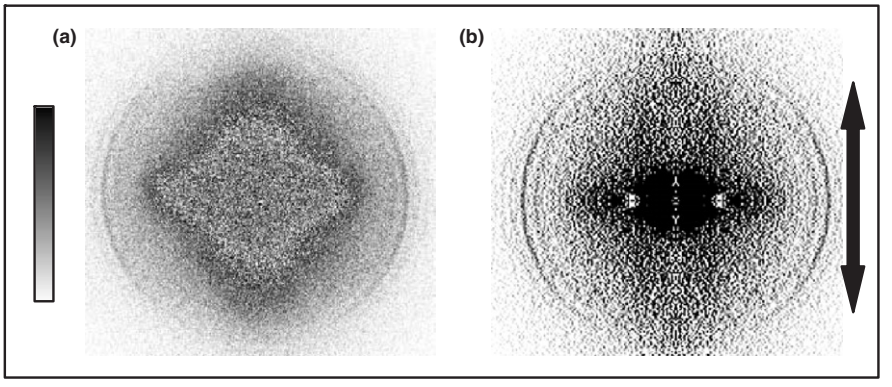

Figure 9. Doppler-free (a) and corresponding Abel inverted image (b) of $D(^2S)$ formed from the one-photon dissociation of vibrationally excited OD $X\,^2\Pi$ radicals at $\approx$243 nm. See Figure 3 for other details.

$1^2\Sigma^-$ state, as in the case of OH. Their experimental β parameters for the three spin–orbit products $S(^3P_J)$ have the same -1 value in the 216–232 nm region, which is similar to the results from this present study (for $O(^3P_0)$ and $D(^2S)$) where the anisotropy parameters are also nearly energy-independent. We should also point out that our uncertainties in branching ratios and angular distribution parameters are relatively large, due to the very small populations of the vibrationally excited molecules studied in this work. Good agreement is found for the sudden limit predictions, but it would still be worthwhile to use a different experimental approach (such as VUV photodissociation) in order to obtain a higher experimental precision for a more stringent comparison with theory.

7. Conclusion

While the photodissociation of OH/OD is energetically allowed above 4.37 eV ($\lambda < 284$ nm), Franck-Condon overlap restricts absorption from the X ground state $v''=0$ to $\lambda < \sim 180$ nm. When OH is populated in higher vibrational levels, however, UV radiation can excite the molecules into the direct dissociation $1^2\Sigma^-$ continuum, leading to the observed H/D and O atom product signals. An estimate of $\approx$2000 K for the vibrational temperature of the pulsed discharge beam source of OH was obtained by comparing the relative signal levels from photodissociation from different vibrational levels with theoretical predictions of the absorption cross- section. The fragment angular distributions for the $D(^2S)$ and $O(^3P_0)$ fragments, which are not complicated by atomic angular momentum alignment effects, indicate a pure perpendicular molecular dissociation, as expected for a $1^2\Sigma^- \leftarrow X^2\Pi$ dissociation process. The measured $O(^3P_J)$ product branching ratios are constant, within our error limits, for the dissociation wavelengths 243 nm, 226 nm, 205 nm, and 200 nm, with a $\approx 5:3:1$ ratio for $J=2:1:0$, as predicted theoretically for a sudden limit diabatic dissociation process. In the sudden limit the M_J distribution for a given J state is quite non-statistical, and this introduces a strong angle-dependent probability for ionization by the linearly polarized probe laser. The measured angular distribution parameters β and γ for the $O(^3P_{2,1})$ product atoms are predicted reasonably accurately by the sudden limit theoretical treatment. The values for these angular distribution parameters are, like the $O(^3P_J)$ branching ratios, independent of dissociation wavelength, which is to be expected for photodissociation in the sudden limit regime. Experimental complications such as ion-recoil from the photoionization step and possible OH pre-orientation and alignment due to the hexapole focusing method were also discussed.

Acknowledgements

This work is part of the research programme of the 'Stichting voor Fundamenteel Onderzoek der Materie (FOM)', which is financially supported by the 'Nederlandse Organisatie voor Wetenschappelijk Onderzoek (NWO)'. The *ab initio* work has been financially supported by the Council for Chemical Sciences of the Netherlands Organization for Scientific Research (CW-NWO).

References

[1] D.Č. Radenović, A.J.A. Van Roij, D.A. Chestakov, *et al.*, J. Chem. Phys. **119**, 9341 (2003).
[2] W. Zhou, Y. Yuan, and J. Zhang, J. Chem. Phys. **119**, 9989 (2003).
[3] M.C. Abrams, S.P. Davis, M.L.P. Rao, *et al.*, J. Mol. Spectrosc. **165**, 57 (1994).
[4] E.F. Dishoeck and A. Dalgarno, J. Chem. Phys. **79**, 873 (1983).
[5] W.G. Roberge, A. Dalgarno, and B.P. Flannery, Astrophys. J. **243**, 817 (1981).
[6] E.F. van Dishoeck, S.R. Langhoff, and A. Dalgarno, J. Chem. Phys. **78**, 4552 (1983).
[7] M.C. van Beek and J.J. ter Meulen, Chem. Phys. Lett. **337**, 237 (2001).
[8] A.T.J.B. Eppink and D.H. Parker, Rev. Sci. Instrum. **68**, 3477 (1997).
[9] L.M.C. Janssen, M.P.J. van der Loo, G.C. Groenenboom, *et al.*, J. Chem. Phys. **126**, 094304 (2007).
[10] W. Zhou, Y. Yuan, S. Chen, and J. Zhang, J. Phys. Chem. **128**, 054330 (2005).
[11] M.P.J. Van der Loo and G.C. Groenenboom, J. Chem. Phys. **123**, 074310 (2005).
[12] G.H. Dieke and H.M. Crosswhite, J. Quantum Radiat. Transfer. **2**, 97 (1962).
[13] D.R. Yarkony, J. Chem. Phys. **97**, 1838 (1992).
[14] C. Kalyanaraman and N. Sathyamurthy, Chem. Phys. **187**, 219 (1994).
[15] S.Y. Lee, J. Chem. Phys. **103**, 3501 (1995).
[16] M.E. Greenslade, M.I. Lester, D.Č. Radenović, *et al.*, J. Chem. Phys. **123**, 074309 (2005).
[17] MOLPRO, version 2006.1, a package of *ab initio* programs, H.-J. Werner, P. J. Knowles, R. Lindh, F. R. Manby, M. Schütz, P. Celani, T. Korona, G. Rauhut, R. D. Amos, A. Bernhardsson, A. Berning, D. L. Cooper, M. J. O. Deegan, A. J. Dobbyn, F. Eckert, C. Hampel and G. Hetzer, A. W. Lloyd, S. J. McNicholas, W. Meyer and M. E. Mura, A. Nicklass, P. Palmieri, R. Pitzer, U. Schumann,

H. Stoll, A. J. Stone, R. Tarroni and T. Thorsteinsson, see http://www.molpro.net.
[18] P.J. Knowles and H.J. Werner, Chem. Phys. Lett. **145**, 514 (1988).
[19] H.J. Werner and P.J. Knowles, J. Chem. Phys. **89**, 5803 (1988).
[20] H.J. Werner and P.J. Knowles, J. Chem. Phys. **82**, 5053 (1985).
[21] P.J. Knowles and H.J. Werner, Chem. Phys. Lett. **115**, 259 (1985).
[22] D.T. Colbert and W.H. Miller, J. Chem. Phys. **96**, 1982 (1992).
[23] G.C. Groenenboom and D.T. Colbert, J. Chem. Phys. **99**, 9681 (1993).
[24] J.B. Lee and L.C. Nee, J. Chem. Phys. **81**, 31 (1984).
[25] M.C.G.N. van Vroonhoven and G.C. Groenenboom, J. Chem. Phys. **116**, 1965 (2002).
[26] Y. Mo, H. Katayanagi, M.C. Heaven, *et al.*, Phys. Rev. Lett. **77**, 830 (1996).
[27] S.J. Singer, K.F. Freed, and Y.B. Band, J. Chem. Phys. **79**, 6060 (1983).
[28] K. Schreel and J.J. ter Meulen, J. Phys. Chem. A. **101**, 7639 (1997).
[29] J. Luque and D.R. Crosley, LIFBASE: Database and Spectral Simulation Program (Version 1.5). SRI International Report No. MP 99-009 (1999).
[30] E. de Beer, M.P. Koopmans, C.A. De Lange, *et al.*, J. Chem. Phys. **94**, 7634 (1991).
[31] A.M. Coroiu, D.H. Parker, G.C. Groenenboom, *et al.*, Eur. J. Phys. D. **38**, 151 (2006).
[32] V. Dribinski, A. Ossadtchi, V.A. Mandelshtam, *et al.*, Rev. Sci. Instrum. **73**, 2634 (2002).
[33] C. Carlone and F. Dalby, Can. J. Phys. **47**, 1945 (1969).
[34] B. Ruscic, D. Feller, D.A. Dixon, *et al.*, J. Phys. Chem. A. **105**, 1 (2001).
[35] M. Cacciatore, M. Capitelli, S. De Benedictis *et al.*, Topics Current Phys. **39**, 5 (1986); M. Capitelli, C. Gorse, and A. Ricard, *ibid.* **39**, 315 (1986).
[36] J. Fleniken, Y. Kim, and H. Meyer, Chem. Phys. Lett. **318**, 529 (2000).
[37] G.B. Courreges-Lacoste, J.P. Sprengers, J. Bulthuis, *et al.*, Chem. Phys. Lett. **335**, 209 (2001).
[38] M.E. Sanz, M.C. McCarthy, and P. Thaddeus, J. Chem. Phys. **119**, 11715 (2003).
[39] D.H. Parker, R.F. Delmdahl, B.B.L.G. Bakker, *et al.*, J. Chin. Chem. Soc. **48**, 327 (2001).
[40] S. Manzhos, H.P. Loock, B.L.G. Bakker, *et al.*, J. Chem. Phys. **117**, 9347 (2002).
[41] R.L. Toomes, P.C. Samartzis, T.P. Rakitzis, and T.N. Kitsopoulos, Chem. Phys. **301**, 209 (2004).
[42] H.L. Offerhaus, C. Nicole, F. Lépine, *et al.*, Rev. Sci. Instrum. **72**, 3245 (2001).
[43] M.L. Lipciuc and M.H.M. Janssen, Phys. Chem. Chem. Phys. 8, 3007 (2006); D.A. Chestakov, M. Wu, G. Wu *et al.*, J. Phys. Chem A. **108**, 8100 (2004).
[44] A.E. Pomerantz and R.N. Zare, Chem. Phys. Lett. **370**, 515 (2003).
[45] T.P. Rakitzis, A.J. van den Brom, and M.H.M. Janssen, Science. **303**, 1852 (2004).
[46] M.C. van Beek, J.J. ter Meulen, and M.H. Alexander, J. Chem. Phys. **113**, 637 (2000).
[47] S.Y. Lee, J. Chem. Phys. **111**, 6407 (1999).